steel research international
www.steel-research.de

Computational Fluid Dynamics Simulation of Iron Ore Reduction in Industrial-Scale Fluidized Beds

Simon Schneiderbauer, Mustafa Efe Kinaci, and Franz Hauzenberger*

Detailed simulations of industrial-scale fluidized beds such as the FINEX process are still unfeasible due to the wide range of spatial scales. Due to the computational limitations it is common to apply coarse grids, which do not resolve all relevant structures. In our previous study (Schneiderbauer, *AIChE J.* 2017, *63*, 3562), we have presented subgrid models, which enable the coarse grid simulation of dense large-scale gas–solid flows. Herein, these corrections are applied to a parcel-based the dense discrete phase model (DDPM), allowing to study the hydrodynamics of the FINEX process. Furthermore, the parcel approach is augmented by an unreacted shrinking core model (USCM) to account for the direct reduction of the iron ore particles by the reducing agents of H_2 and CO. This DDPM model is tested first for a cold pilot-scale fluidized bed, and second, the USCM approach is validated for the direct reduction in a lab-scale fluidized bed. Finally, the model is applied to the FINEX process. The results show fairly good agreement with measurements of the average bed voidage and with experimentally determined particle size distributions. The results further indicate that fines are immediately reduced, whereas the reduction of the largest ore grains takes considerably longer.

1. Introduction

The main conversion process to gain metallic iron from oxidic iron compounds is the reduction of iron ores by suitable reducing agents, where iron oxides are reduced to metallic iron by gaseous reducing agents (CO and H_2). During the reduction of iron ores, oxygen is removed according to the thermodynamic equilibrium conditions, until the next oxidation level is reached. The gaseous reduction of iron oxides and the oxidation of the reducing agents can be described by the following reaction mechanism[1]

$$Fe_xO_y + yCO \rightarrow xFe + yCO_2 \tag{1}$$

$$Fe_xO_y + yH_2 \rightarrow xFe + yH_2O \tag{2}$$

These equations reveal that the reduction reactions of iron ores can be considered as elementary reactions, which means that the number of moles of the gaseous components does not change during the reactions. The leading process used in iron-making is the blast furnace, which consists of a moving bed reactor with countercurrent flow of the solid reactants against a reducing gas. In the lower part the iron is molten and carburized. However, in the blast furnace process iron ore fines, which build up around 80% of the total iron ore, need to go through a preparation step (i.e., pelletizing or sintering process[2]). In contrast, by using fluidized bed technology fine ores can directly be charged into the reduction process. Such fluidized bed reactors are used, for example, in the FINEX process.[3,4] The FINEX process, which was jointly developed by POSCO (Korea) and Primetals Technologies (Austria), produces hot metal in the same quality as traditional blast furnaces; however, the coke making and sintering of the fine ores are avoided. The iron ores that are charged into the process go through fluidized bed reactors where they are heated and reduced to direct reduced iron (DRI), charged into the melter gasifier, where final reduction and melting as well as the production of reducing gas by gasification of coal with oxygen take place.[5] Another advantage of the FINEX process is the exhaust gas, which can be used for various other applications such as heating within a steel plant as, for example, power generation. More detailed information can be found in ref. [4].

Due to the limited accessibility for measurements, simulation methods have become one of the most important tools for optimizing the iron making processes.[1,6–9] However, either these numerical models neglect the impact of the reduction of iron ore[9] or these are restricted to very small-scale processes such as individual pellets,[1,8,10] lab-scale fluidized beds,[6,7,11,12] or small packed beds.[13–15] It has to be noted that the latter utilized the CFD-DEM approach (Euler–Lagrange approach) to model the gas–solid flow, where the continuous phase is governed by computational fluid dynamics (CFD) and the particle trajectories

---

Dr. S. Schneiderbauer, M. E. Kinaci
Christian Doppler Laboratory for Multi-scale Modelling of Multiphase Processes
Johannes Kepler University
Altenbergerstraße 69, 4040 Linz, Austria
E-mail: simon.schneiderbauer@jku.at

F. Hauzenberger
UP I&S DR TI
Primetals Technologies Austria GmbH
Turmstraße 44, 4031 Linz, Austria

The ORCID identification number(s) for the author(s) of this article can be found under https://doi.org/10.1002/srin.202000232.

DOI: 10.1002/srin.202000232

are computed by using the discrete element method (DEM), which is rather computationally demanding.[16,17]

As the total number of particles in fluidized bed reactors is extremely large, it may be impractical to solve the equations of motion for each particle. It is, therefore, common to investigate particulate flows in large process units using averaged equations of motion, i.e., two-fluid models (TFMs; Euler–Euler approach), which include the interparticle collisions statistically by kinetic theory-based closures of the particle stresses.[18–20] However, industrial processes commonly include broad particle size distributions. In the context of the Euler–Euler approach, each representative particle diameter requires an additional momentum and continuity equation (multifluid model), which considerably raises the computational demand with increasing number of particle diameters.[21,22] Here, one may restrict the calculations to spatially constant particle size distributions to evaluate the gas–solid drag force.[23]

To overcome these deficiencies of CFD-DEM and the multifluid models, we use the dense discrete phase model (DDPM).[24–32] Here, particle–particle interactions are represented by models which use mean values calculated on the Eulerian mesh. Thus, not every particle and its interactions are calculated, which significantly reduces the computational cost.[28–30,33–37] Furthermore, particles are grouped into computational parcels with the same velocities and properties, which further allows a considerable reduction of the computational costs.[38] A second advantage of the DDPM is that the representation of the particle phase is still of Lagrangian nature. This, in turn, implies that particle size distributions and gas–particle reaction can be easily incorporated.

Although the DDPM model requires much less computational resources compared with CFD-DEM as well as a multifluid model, it is still computationally challenging to assess industrial-scale processes. The DDPM approach nonetheless requires very fine computational meshes to resolve all relevant heterogeneous structures occurring in gas–solid flows, such as clusters and streamers.[39,40] Consequently, grid coarsening significantly reduces the computational demands, but inevitably neglects the small structures and thus leads to an incorrect prediction of the hydrodynamics of gas–solid flows.[41,42] Here, the gas–solid drag force has to be outlined as the most significant contribution.[43] Many subgrid drag modifications have, therefore, been proposed to account for the effect of these small meso-scale structures on the resolved macroscales.[41–49] It has to be noted that most of those models have been developed in the context of the Euler–Euler approach, but it is agreed that these are also applied to Euler–Lagrange simulations.[40,50] Recently, we have presented a novel approach for deriving constitutive relations for the unresolved terms appearing in coarse grid simulations. Thereby, we advanced a spatially averaged two-fluid model (SA-TFM), which is based on the concepts of turbulence modeling.[51–58] This approach appears to be more general than the functional fitting approach used in the literature.[53]

In this article, we present a parcel-based Euler–Lagrange approach (aka DDPM), which accounts for the unresolved heterogeneous gas–solid structures by using subgrid models derived in our previous work.[51–56] Furthermore, this approach is verified in the case of a pilot-scale bubbling fluidized bed and the impact of subgrid structures is discussed. Subsequently, we combine the present DDPM approach with a particle-based model for the direct reduction of iron ores, which has been proposed in our previous work.[12] This combined method is applied to the reduction of hematite ore in a lab-scale fluidized bed and an industrial-scale fluidized bed (FINEX). Finally, a conclusion and outlook section ends this article.

2. Numerical Modeling

2.1. Dense Discrete Phase Model

The DDPM formulation is based on the governing equations of a TFM approach. However, in contrast to TFM the particle phase equations are discretized by using Lagrangian parcels (representing a certain amount of solid), where the parcel properties are projected to the Eulerian grid.[25–32] Thus, the continuity, momentum, energy, and species transport equations for the gaseous phase f are given by

$$\frac{\partial}{\partial t}(\epsilon_f \rho_f) + \nabla \cdot (\epsilon_f \rho_f \boldsymbol{u}_f) = S_m \tag{3}$$

$$\begin{aligned}\frac{\partial}{\partial t}(\epsilon_f \rho_f \boldsymbol{u}_f) + \nabla \cdot (\epsilon_f \rho_f \boldsymbol{u}_f \boldsymbol{u}_f) = -\epsilon_f \nabla p + \nabla \cdot \tau_f \\ + K_{\mathrm{DPM}}(\boldsymbol{u}_s - \boldsymbol{u}_f) + \epsilon_f \rho_f \boldsymbol{g} + \boldsymbol{S}_{\mathrm{mom}}\end{aligned} \tag{4}$$

$$\begin{aligned}\frac{\partial}{\partial t}(\epsilon_f \rho_f h_f) + \nabla \cdot (\epsilon_f \rho_f \boldsymbol{u}_f h_f) = \epsilon_f \frac{\partial p}{\partial t} + \tau_f : \nabla \boldsymbol{u}_f - \nabla \cdot \boldsymbol{q}_f \\ - \nabla \cdot \left[\epsilon_f \sum_{k=1}^{m} h_{f,k} \boldsymbol{J}_k \right] + S_h\end{aligned} \tag{5}$$

$$\frac{\partial}{\partial t}(\epsilon_f \rho_f Y_{f,k}) + \nabla \cdot (\epsilon_f \rho_f \boldsymbol{u}_f Y_{f,k}) = \nabla \cdot \epsilon_f \boldsymbol{J}_k + R_k \tag{6}$$

In Equation (3)–(6) ϵ_f, ρ_f, and $\boldsymbol{u}_f$ denote the void fraction, density, and velocity of the fluid phase. Furthermore, p is the gas-phase pressure, $\tau_f(= 2\mu_f[\nabla \boldsymbol{u}_f + (\nabla \boldsymbol{u}_f)^t])$ is the gas-phase shear stress tensor with μ_f being the molecular viscosity, and $\boldsymbol{g}$ is the gravitational acceleration; h_f denotes the specific enthalpy and $\boldsymbol{q}_f$ is the heat flux; $Y_{f,k}$ stands for a gaseous species (such as CO, CO_2, etc.) with index k, whereas m is the number of species in the gaseous phase and $\boldsymbol{J}_k$ is the diffusion flux of species k. Finally, R_k represents the net rate of production/consumption of species k due to heterogeneous reactions. S_m, $\boldsymbol{S}_{\mathrm{mom}}$, and S_h are sources of mass, momentum, and enthalpy due to those heterogeneous reactions. The energy source S_h furthermore accounts for the convective heat transfer between gas phase and the discrete solid phase, where we use the model of Gunn.[59] It has to be emphasized that in this article heat transfer due to radiation is not considered.

The set of gas-phase equations (Equation (3)–(6)) is augmented by the equations of motion for the solid phase particles

$$\frac{d\boldsymbol{u}_p}{dt} = F_D(\boldsymbol{u}_f - \boldsymbol{u}_p) + \frac{\rho_p - \rho_f}{\rho_p} \boldsymbol{g} - \frac{1}{\rho_p} \nabla \cdot \sigma_s \tag{7}$$

with $\boldsymbol{u}_p$ being the velocity of particle p, ρ_p being the particle density, and F_D being the drag coefficient. In this work, we use the drag model of Beetstra et al.[60] accounting for polydisperse particle mixtures. For brevity, the details are not repeated here and can be found elsewhere.[11,23,38,60,61] In contrast to the DEM,[61] where particle–particle collisions are resolved by a contact model,[62,63] these interactions are included by the last term in Equation (7). Here, σ_s denotes the solids stress, which on average determines the impact of all individual collisions. In the DDPM, σ_s is usually closed by using the kinetic theory of granular flows (KTGF),[24] but also other stress models are used in the literature.[34,39,64] However, in general the evaluation of the solids stress tensor requires Eulerian field quantities such as volume fraction and solid velocity $\boldsymbol{u}_s$, which can be determined from projecting the Lagrangian tracking information on the Eulerian grid used for the solution of Equation (3)–(6). Finally, the drag coefficient K_{DPM} appearing in Equation (4) is computed from a local cell average of the drag coefficient used in Equation (7).

2.2. Spatially Averaged DDPM

Due to computational limitations, a highly resolved simulation of industrial-scale reactors is still unfeasible.[43,65] Euler–Lagrange methods commonly require at least a grid spacing, which is approximately 3–4 times the particle diameter.[38,50] It is, therefore, straightforward to apply coarse grids, which allow a considerable reduction of the computational effort. Nevertheless, such a procedure does not resolve all relevant flow features by Equations (3)–(6).

In addition, tracking all particles individually is commonly not feasible. Thus, it is quite common to simulate only a subset of particles (parcels), where each simulated particle is a proxy for a prescribed number of real particles (a.k.a. parcel size).[38] The former coarsening strategies is commonly referred to as "grid coarsening," whereas the latter is denoted by "particle coarsening."[38]

Mathematically, grid coarsening can be described by applying a spatial filter operation to Equations (3)–(6), which gives their filtered (discretized or resolved) counterpart. It has to be noted that in this article we solely consider the impact of grid coarsening on the hydrodynamics and not on heat and mass transfer because in the case of iron ore reduction the reaction rates are mostly dependent on the grain structure.[1,12] It is expected that the heterogeneous subfilter distribution of the species concentrations has only a minor impact on the reaction rates.

The filtered complement of a continuous space–time variable $g(x_i, t)$ is given by

$$\bar{g}(\boldsymbol{x}, t) = \mathcal{G}g \tag{8}$$

where $\mathcal{G}$ denotes the filter operator defined by the convolution of $g(\boldsymbol{x}, t)$ with a weighting function $G(\boldsymbol{x}, \boldsymbol{y}, \Delta_{fi})$ satisfying $\int G\mathrm{d}V = 1$. Thus, $\bar{g}(\boldsymbol{x}, t)$ is determined by

$$\bar{g}(\boldsymbol{x}, t) = G \star g(\boldsymbol{x}, t) = \int G(\boldsymbol{x}, \boldsymbol{y}, \Delta_{fi}) g(\boldsymbol{x}, t) \mathrm{d}V_y \tag{9}$$

where Δ_{fi} denotes the filter width and $\mathcal{G} \equiv (G\star)$. Applying Equation (9) to Equation (3) and (4) yields

$$\frac{\partial}{\partial t}(\bar{\epsilon}_f \rho_f) + \nabla \cdot (\bar{\epsilon}_f \rho_f \langle \boldsymbol{u}_f \rangle_f) = \bar{S}_m \tag{10}$$

$$\begin{aligned} &\frac{\partial}{\partial t}(\bar{\epsilon}_f \rho_f \langle \boldsymbol{u}_f \rangle_f) + \nabla \cdot (\epsilon_f \rho_f \langle \boldsymbol{u}_f \rangle_f \langle \boldsymbol{u}_f \rangle_f) = \\ &\quad - \bar{\epsilon}_f \nabla \bar{p} + \nabla \cdot \bar{\tau}_f - \nabla \cdot R_f + \tilde{K}_{\mathrm{DPM}}(\tilde{\boldsymbol{u}}_s - \langle \boldsymbol{u}_f \rangle_f) + \bar{\epsilon}_f \rho_f \boldsymbol{g} \end{aligned} \tag{11}$$

where we used Favre averages

$$\langle \boldsymbol{u}_f \rangle_f = \frac{\overline{\epsilon_f \boldsymbol{u}_f}}{\bar{\epsilon}_f} \tag{12}$$

The Reynolds-stress-like contribution stemming from the convective term reads

$$R_f = \bar{\epsilon}_f \rho_f (\langle \boldsymbol{u}_f \boldsymbol{u}_f \rangle_f - \langle \boldsymbol{u}_f \rangle_f \langle \boldsymbol{u}_f \rangle_f) \tag{13}$$

Applying particle coarsening to the equation of motion of the solid particles (7) reveals

$$\frac{\mathrm{d}\tilde{\boldsymbol{u}}_p}{\mathrm{d}t} = (1 - c)\tilde{F}_D(\langle \boldsymbol{u}_f \rangle_f - \tilde{\boldsymbol{u}}_p) + \frac{\rho_p - \rho_f}{\rho_p}\boldsymbol{g} - \frac{1}{\rho_p}\nabla \cdot \tilde{\sigma}_s - \frac{1}{\rho_p}\nabla \cdot R_s \tag{14}$$

with $\tilde{\boldsymbol{u}}_p$ being the parcel velocity. In the following, $\tilde{}$ represents parcel properties, such as the solid stress tensor $\tilde{\sigma}$, which is derived from the parcel trajectories. Furthermore, R_s is the Reynolds-stress-like contribution to the solids stress, which arises from the unresolved dispersion of particles due to particle coarsening. Finally, c is the fractional correction representing the reduction of the gas–solid drag force stemming from unresolved heterogeneous structures.[43–47,51,52,57,58,66] On the one hand, during the grid coarsening step the spatial structure of small clusters and streamer is lost. On the other hand, particle coarsening neglects the impact of the particle velocity distribution on the averaged drag force. Following Rauchenzauner and Schneiderbauer,[52] the fractional correction can be written as

$$c = -\frac{\overline{(1 - \epsilon'_f)\boldsymbol{u}''_f}}{\bar{\epsilon}_f (1 - \bar{\epsilon}_f) \| \langle \boldsymbol{u}_f \rangle_f - \tilde{\boldsymbol{u}}_p \|} \tag{15}$$

where $\epsilon'_f = \epsilon_f - \bar{\epsilon}_f$ and $\boldsymbol{u}''_f = \boldsymbol{u}_f - \langle \boldsymbol{u}_f \rangle_f$. The covariance $\overline{(1 - \epsilon'_f)\boldsymbol{u}''_f}$ can be approximated by

$$\overline{(1 - \epsilon'_f)\boldsymbol{u}''_f} = \xi_{f\epsilon}\sqrt{2k_f\overline{\phi'^2}} \tag{16}$$

with the correlation coefficient $\xi_{f\epsilon}$, the turbulent kinetic energy of the gas phase k_f, and the variance of the void fraction $\overline{\phi'^2}$. A good approximation for the correlation coefficient is given by[53]

$$\xi_{f\epsilon} = -0.5\bar{\epsilon}_f \tag{17}$$

Closure models for the Reynolds-stress-like contributions are given by[51]

$$R_f = \bar{\epsilon}_f \rho_f \left(\frac{2}{3}k_f I - 2\mu_{f,t}\widehat{S}_f\right) \tag{18}$$

$$R_s = (1 - \bar{\epsilon}_f)\rho_p \left(\frac{2}{3}k_s I - 2\mu_{s,t}\widehat{S}_s\right) \tag{19}$$

It has to be emphasized that we already discussed the constitutive relations for k_s, k_f, $\mu_{f,t}$, $\mu_{s,t}$, and $\overline{\phi'^2}$ in detail previously, and thus we do not discuss them here. These can be found in our previous work.[51,52,54] Finally, the drag coefficient $\tilde{K}_{\mathrm{DPM}}$ appearing in Equation (11) is computed from a local cell average of the drag coefficient $(1 - c)F_D$ used in Equation (14).

2.3. Modeling Direct Reduction of Iron Ore

The main reactions for the reduction of metallic oxide with a gaseous reductant of carbon monoxide (CO) and hydrogen (H_2) can be expressed with the following steps:[1,8,12]

Hematite to magnetite:

$$3Fe_2O_3 + CO/H_2 \rightarrow 2Fe_3O_4 + CO_2/H_2O \tag{20}$$

Magnetite to wustite:

$$Fe_3O_4 + CO/H_2 \rightarrow 3FeO + CO_2/H_2O \tag{21}$$

Wustite to iron:

$$FeO + CO/H_2 \rightarrow Fe + CO_2/H_2O \tag{22}$$

If the reaction temperature is below 570 °C, then there is no wustite formation and magnetite reduces directly to metallic iron with the reaction

$$0.25Fe_3O_4 + CO/H_2 \rightarrow 0.75Fe + CO_2/H_2O \tag{23}$$

2.3.1. Reaction Kinetics

The most common types of representation models for the noncatalytic reactions of solids submerged in fluids are the shrinking particle model (SPM) and the unreacted shrinking core model (USCM),[12] where the USCM is accepted as the most precise model to represent direct reduction of iron ore.[1,8] In particular, in this work we use a three-layer USCM to represent the three interfaces of hematite/magnetite, magnetite/wustite, and wustite/iron (**Figure 1**a). For further details about the three-layer USCM, the reader is referred to our previous work.[12]

According to Tsay et al.[67] the removal rate of oxygen is determined through the following mechanisms: 1) the reducing gas is transported through the gas film onto the particle surface (F); 2) diffusion through the porous iron layer (B_{Fe}); 3) reactants react with wustite at the wustite/iron interface and form iron (A_{wFe}); 4) remaining reactants diffuse through the wustite layer to the wustite/magnetite interface (B_w); 5) reaction with magnetite at layer surface forming wustite and gaseous products (A_{mw}); 6) remaining reactants diffuse through the magnetite layer to the magnetite/hematite interface (B_m); 7) reaction with hematite core forming magnetite and a gaseous products (A_{hm}); and 8) the gaseous products diffuse outward through the pores of the pellet.

As each step is a resistance to the total reduction of the pellet, the reduction pattern of a single particle can be considered to follow a resistance network such as an electrical resistance circuit network (Figure 1b). The solution of this resistance network yields the reaction flow rate of $\frac{\mathrm{d}m_k^{ij}}{\mathrm{d}t}$ of the gas species for the relative layers yields

$$\begin{aligned}\frac{\mathrm{d}m_k^{hm}}{\mathrm{d}t} = \frac{1}{RT_p}\frac{4\pi r_p^2}{W_{hm}}\nu_k M_k\Big\{&[A_{wFe}(A_{mw} + B_w + B_{Fe} + F)\\ &+ (B_{Fe} + F)(A_{mw} + B_w)](p_k - p_{k,\mathrm{eq}}^{hm})\\ &- [A_{wFe}(B_w + B_{Fe} + F) + B_w(B_{Fe} + F)]\\ &\times (p_k - p_{k,\mathrm{eq}}^{mw}) - [A_{mw}(B_{Fe} + F)](p_k - p_{k,\mathrm{eq}}^{wFe})\Big\}\end{aligned} \tag{24}$$

$$\begin{aligned}\frac{\mathrm{d}m_k^{mw}}{\mathrm{d}t} = \frac{1}{RT_p}\frac{4\pi r_p^2}{W_{hm}}\nu_k M_k\Big\{&[(A_{hm} + B_m + B_w)(A_{wFe} + B_{Fe} + F)\\ &+ A_{wFe}(B_{Fe} + F)](p_k - p_{k,\mathrm{eq}}^{mw}) - [B_w(\mathrm{A}_{wFe} + B_{Fe} + F)\\ &+ A_{wFe}(B_{Fe} + F)](p_k - p_{k,\mathrm{eq}}^{hm})\\ &- [(A_{hm} + B_m)(B_{Fe} + F)](p_k - p_{k,\mathrm{eq}}^{wFe})\Big\}\end{aligned} \tag{25}$$

$$\begin{aligned}\frac{\mathrm{d}m_k^{wFe}}{\mathrm{d}t} = \frac{1}{RT_p}\frac{4\pi r_p^2}{W_{hm}}\nu_k M_k\Big\{&[(A_{hm} + B_m)(A_{mw} + B_w + B_{Fe} + F)\\ &+ A_{mw}(B_w + B_{Fe} + F)](p_k - p_{k,\mathrm{eq}}^{wFe})\\ &- [A_{mw}(B_{Fe} + F)](p_k - p_{k,\mathrm{eq}}^{hm})\\ &- [(A_{hm} + B_m)(B_{Fe} + F)](p_k - p_{k,\mathrm{eq}}^{mw})\Big\}\end{aligned} \tag{26}$$

where

$$\begin{aligned}W_{hm} = (A_{hm} + B_{hm})&[A_{wFe}(A_{mw} + B_w + B_{Fe} + F)\\ &+ (A_{mw} + B_m)(B_w + F)]\\ &+ A_{mw}[A_{wFe}(B_m + B_w + F) + B_w(B_{Fe} + F)]\end{aligned} \tag{27}$$

In Equation (24)–(26), R is the universal gas constant, T_p is the temperature of the particle, r_p is the diameter of the particle, ν_k is the stoichiometric coefficient of reactant gas species k, M_k

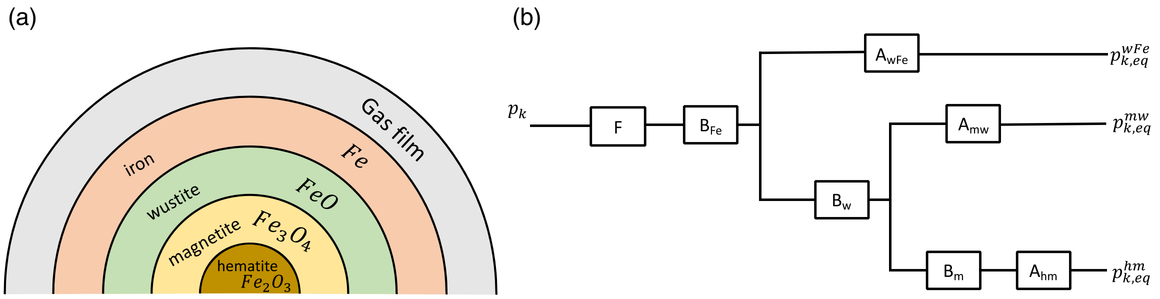

Figure 1. a) A schematic of the three-layer USCM;[12] b) the visualization of the stepwise reduction of iron oxide as an electrical circuit network, where the resistances due to chemical reactions are represented as A, diffusion resistances through individual layers as B, and the resistance due to mass transfer through the gas film as F. $p_{k,\mathrm{eq}}^{wFe}$ denotes the equilibrium partial pressure at the wustite–iron interface, $p_{k,\mathrm{eq}}^{mw}$ denotes the equilibrium partial pressure at the hematite–wustite interface, and $p_{k,\mathrm{eq}}^{hm}$ denotes the equilibrium partial pressure at the hematite–magnetite interface.

is the molecular weight of reactant gas species k, p_k is the partial pressure of reactant gas species k, and $p_{k,\mathrm{eq}}^{ij}$ is the equilibrium partial pressure for gas species k for reaction $i \rightarrow j$ with $i,j \in \{h, m, Fe\}$.

The mass change rate per reaction step for the other species in the reactions shown in Equation (20)– (22) can be determined with the mass reduction rate of reactant gas as

$$R_n \equiv \frac{\mathrm{d}m_n^{ij}}{\mathrm{d}t} = \frac{\mathrm{d}m_k^{ij}}{\mathrm{d}t}\frac{\nu_j}{\nu_k}\frac{M_j}{M_k} \tag{28}$$

where n represents the solid and gas species taking part in reaction $i \rightarrow j$ with gas species k. The resistances appearing in Figure 1b and in Equation (24)–(27) and affecting the overall reaction rate can be expressed as[1,12]

$$A_{ij,k} = \left[\frac{1}{k_i}(1-f_i)^{-\frac{2}{3}}\frac{K_{\mathrm{eq},i}}{1+K_{\mathrm{eq},i}}\right]_k \tag{29}$$

$$B_{i,k} = \left[\left((1-f_i)^{-\frac{1}{3}} - (1-f_{i+1})^{-\frac{1}{3}}\right)\frac{r_p}{D_{\mathrm{eff},i}}\right]_k \tag{30}$$

$$F_k = \left[\frac{1}{\beta_i}\right]_k \tag{31}$$

In the aforementioned equation, $K_{\mathrm{eq},i}$ is the equilibrium constant of the layer i (Figure 1a). These equilibrium constants are commonly deduced from the so-called Baur–Glaessner diagram.[12] In such a diagram, the stability regions for the different iron oxides and iron phases are depicted as a function of temperature and CO/CO_2 as well as H_2/H_2O mixtures. Appropriate correlations for $K_{\mathrm{eq},i}$ are found in our previous study.[12] Furthermore, k_i is the kinetic constant of each reduction layer that is determined by an Arrhenius-type equation

$$k_i = k_{0,i}\exp\left(-\frac{E_i}{RT_p}\right) \tag{32}$$

The kinetic parameters, which consist of the preexponential factor $k_{0,i}$ and the activation energy E_i. Corresponding values for the hematite ore used in this study can be found in ref. [12].

The term $f_i$denotes the fraction reduction of layer i, which is the ratio of mass loss of the oxygen removed in layer i to the total mass of removable oxygen. The fractional reduction for the different reduction steps is defined as

$$\begin{aligned}
f_h &= 1 - \frac{\frac{2m_{\mathrm{Fe_2O_3}}}{M_{\mathrm{Fe_2O_3}}}}{\frac{2m_{\mathrm{Fe_2O_3}}}{M_{\mathrm{Fe_2O_3}}} + \frac{3m_{\mathrm{Fe_3O_4}}}{M_{\mathrm{Fe_3O_4}}} + \frac{m_{\mathrm{FeO}}}{M_{\mathrm{FeO}}} + \frac{m_{\mathrm{Fe}}}{M_{\mathrm{Fe}}}}\\
f_m &= 1 - \frac{\frac{2m_{\mathrm{Fe_2O_3}}}{M_{\mathrm{Fe_2O_3}}} + \frac{3m_{\mathrm{Fe_3O_4}}}{M_{\mathrm{Fe_3O_4}}}}{\frac{2m_{\mathrm{Fe_2O_3}}}{M_{\mathrm{Fe_2O_3}}} + \frac{3m_{\mathrm{Fe_3O_4}}}{M_{\mathrm{Fe_3O_4}}} + \frac{m_{\mathrm{FeO}}}{M_{\mathrm{FeO}}} + \frac{m_{\mathrm{Fe}}}{M_{\mathrm{Fe}}}}\\
f_w &= 1 - \frac{\frac{2m_{\mathrm{Fe_2O_3}}}{M_{\mathrm{Fe_2O_3}}} + \frac{3m_{\mathrm{Fe_3O_4}}}{M_{\mathrm{Fe_3O_4}}} + \frac{m_{\mathrm{FeO}}}{M_{\mathrm{FeO}}}}{\frac{2m_{\mathrm{Fe_2O_3}}}{M_{\mathrm{Fe_2O_3}}} + \frac{3m_{\mathrm{Fe_3O_4}}}{M_{\mathrm{Fe_3O_4}}} + \frac{m_{\mathrm{FeO}}}{M_{\mathrm{FeO}}} + \frac{m_{\mathrm{Fe}}}{M_{\mathrm{Fe}}}}
\end{aligned} \tag{33}$$

Thus, the overall fractional reduction represents the reducible oxygen content and can be deduced from

$$f = \frac{1}{9}f_h + \frac{2}{9}f_m + \frac{6}{9}f_w \tag{34}$$

It has to be emphasized that the conversion rate (Equation (28)) depends on the extent of oxygen due to the reaction resistance $A_{ij,k}$ (Equation (29)), which is a function of the current radius r_i of layer i by

$$f_i = 1 - \left(\frac{2r_i}{d_p}\right)^3 \tag{35}$$

where d_p is the particle diameter. Here, it is assumed that the particle diameter d_p is constant during the conversion process of hematite, magnetite, and wustite, whereas the layer radii (r_h, r_m, and r_w) decrease.[1,12] This, in turn, implies that the removal of oxygen yields lighter and more porous particles with a shrinking core and a growing outer iron layer.

It remains to discuss constitutive relations for the pore and molecular diffusivity, D_{eff}, and the mass transfer coefficient β. However, these are studied extensively in refs. [1,12] which are not repeated here. Finally, the source of gas enthalpy can be computed from

$$S_h = \sum_{k,\,ij}\Delta h_k^{ij}\frac{\mathrm{d}m_k^{ij}}{\mathrm{d}t} \tag{36}$$

where Δh_k^{ij} is the difference of conventional enthalpies for reaction $i \rightarrow j$ with reactant k.

3. Simulations

The commercial CFD code FLUENT 19.2[24] was used for numerical solution of the governing equations. Particularly, we modified FLUENT to account for Equation (10)–(36) by using user-defined functions (UDFs). Pressure–velocity coupling is based on the SIMPLE algorithm. A second-order upwind scheme was used for all variable extrapolation. Time advancement was achieved by a first-order implicit Euler integration for the gas phase and by using a trapezoidal rule for the parcel trajectories.[24]

3.1. Hydrodynamics of Pilot-Scale Bubbling Fluidized Bed

The pilot-scale bubbling fluidized bed consists of a cylinder with 0.267 m inner diameter (**Figure 2**a). This reactor was simulated for comparison with detailed experimental data reported by Zhu et al.[68] The height of the reactor was 2.464 m with an added freeboard region expanding to a height of approximately 4.2 m. The freeboard had an inner diameter of 0.667 m to stop excessive particle entrainment out of the bed. The freeboard region was included in the simulation domain to accurately account for the large degree of bed expansion observed in some of the simulations conducted. Gas was injected through a velocity inlet on the bottom face of the reactor with a superficial gas velocity of $W_g^{\mathrm{in}} = 0.4\,\mathrm{m\,s^{-1}}$. Gas exited at the top of the reactor though a pressure outlet at 0 Pa gauge pressure. We applied a no-slip boundary conditions for the gas phase and an elastic particle rebounds the solid phase at the side walls. The remaining

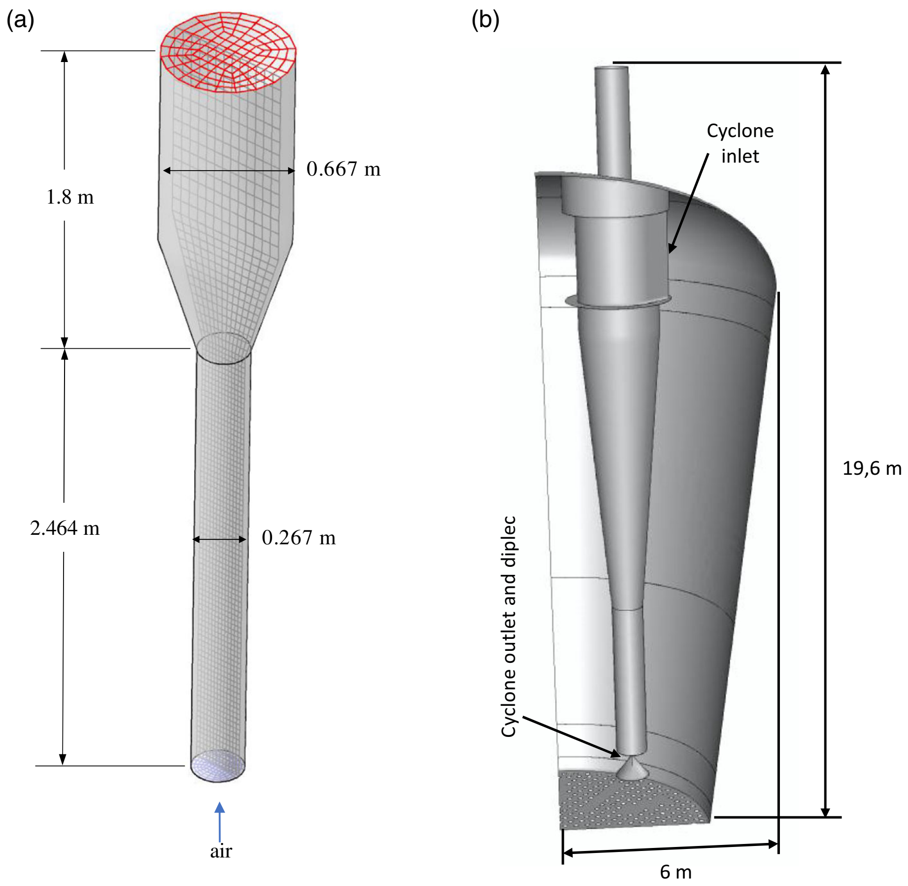

Figure 2. Schematic drawing of a) the pilot-scale fluidized bed and b) the computational model of the industrial-scale fluidized bed.

physical parameters are $r_p = 32.5\,\mu\text{m}$, $\rho_p = 1780\,\text{kg}\,\text{m}^{-3}$, $\rho_f = 1.224\,\text{kg}\,\text{m}^{-3}$, and $\mu_f = 1.78 \times 10^{-5}\,\text{Pa s}$. The solids inventory of 70 kg was represented by about 600 000 parcels. Finally, we used an average grid size of 2 cm, which is about 80 times coarser than the mesh resolution required to resolve all relevant heterogeneous structures.[53,55]

3.2. Iron Ore Reduction in Lab-Scale Fluidized Bed

To validate the presented reduction model, we investigate the direct reduction of hematite ore within a lab-scale fluidized bed with 68 mm diameter.[11,69] Even though the dimensions of the vessel are quite small, we used rather coarse mesh (i.e., ≈5 mm), which does not resolve all relevant heterogeneous structures, and therefore subgrid corrections are required (Section 2.2). Initially, the bed was filled with 0.165 kg hematite ore (Hamersly ore) particles ($\rho_p \approx 4300\,\text{kg}\,\text{m}^{-3}$) following a Rosin–Rammler diameter distribution with an average diameter $d_p = 270\,\mu\text{m}$ and a spreading parameter of 1.48. To increase the initial bed height in the experiments, 0.2 kg of monodispersed inert sand particles with $d_p = 250\,\mu\text{m}$ was added.[12,69] In total, the ore phase was represented by 186 000 parcels, whereas the sand phase was modeled by 18 600 parcels. The pressure in the fluidized bed was 140 000 Pa and the superficial gas velocity $W_g^{\text{in}} = 0.25\,\text{m}\,\text{s}^{-1}$. The detailed inflow conditions for the gas species (CO, CO_2, H_2, H_2O, and N_2) are shown in **Table 1**. It has to be emphasized that the gas composition and gas temperatures are set in such a way that the different reduction occurs sequentially. In particular, during R3 conditions hematite is reduced to magnetite, during R2 magnetite is reduced to wustite, and finally, during R1 wustite is reduced to iron. The inflow gas composition was further matched to the average gas composition occurring in the industrial process.[69] However, it has to be emphasized that in principle the present model is not restricted to such specific operating conditions, but can also be applied to the simultaneous reduction of the different layers.[12]

Table 1. Experimental conditions for the different reduction steps. The concentrations of the reactants are given in volume percent.

	Lab-scale			Large scale
	R3 (H → M)	R2 (M → W)	R1 (W → Fe)	R3 (H → M)
H_2 [%]	13.0	15.9	13.4	14.4
H_2O [%]	6.8	6.8	3.4	7.5
CO [%]	30.3	37.4	37.0	33.6
CO_2 [%]	26.4	27.4	14.0	29.3
N_2 [%]	23.5	12.4	32.2	15.2
T [°C]	480	750	720	480

3.3. Iron Ore Reduction in Industrial-Scale Fluidized Bed (FINEX)

The industrial-scale fluidized bed consists of a nearly cylindrical vessel and four cyclones, which return the smaller entrained particles back to the fluidized bed. A diplec is mounted below the cyclone to avoid a shortcut gas flow through the cyclone. The bed is fluidized due to a grid of nozzles (see Figure 2b) at a Gauge pressure of 331 000 Pa and a superficial gas flow rate of 310000 $\mathrm{Nm^3\,h^{-1}}$. The gas composition is shown in Table 1. The total solids inventory at the initial state is 181 tonnes of hematite ore ($\rho_p \approx 4300\,\mathrm{kg\,m^{-3}}$). The initial particle size distribution is shown in **Figure 3**a. For the numerical simulations, we solely consider one-fourth of the fluidized bed by using the symmetry of the problem (Figure 2b). The solids phase is discretized by using 3 636 983 parcels, whereas we use an average grid spacing of 0.1 m to solve the gas-phase equations. This grid spacing is approximately 100 times larger than the resolution requirement for DDPM,[50] which implies a performance gain of about four orders of magnitude in the case of spatially averaged DDPM (SA-DDPM).

4. Results

4.1. Hydrodynamics of Pilot-Scale Bubbling Fluidized Bed

Figure 4 shows snapshots of the solids volume fraction. The figure clearly shows that the bubbling/slugging regime, which is observed in the experiments,[68] is predicted by the SA-DDPM approach. In contrast, DDPM considerably overestimates the bed expansion.

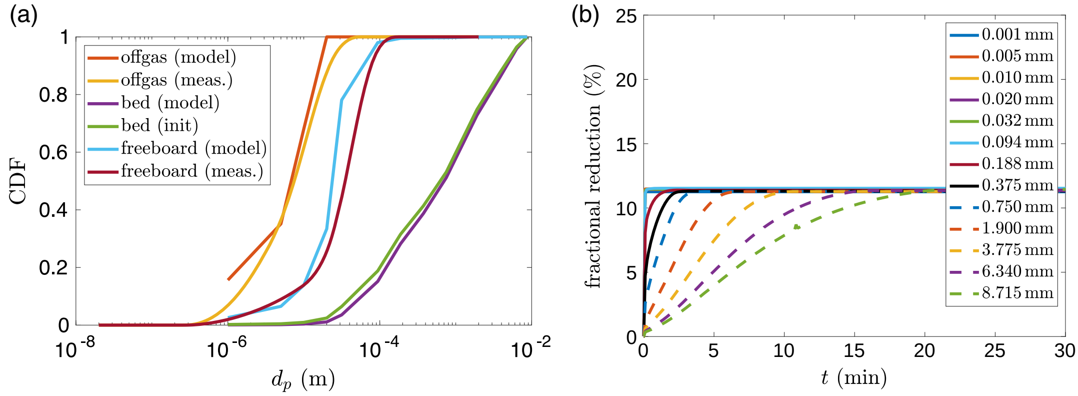

Figure 3. a) Average particle size distributions at different locations; b) fractional reduction as a function of time for different particle sizes.

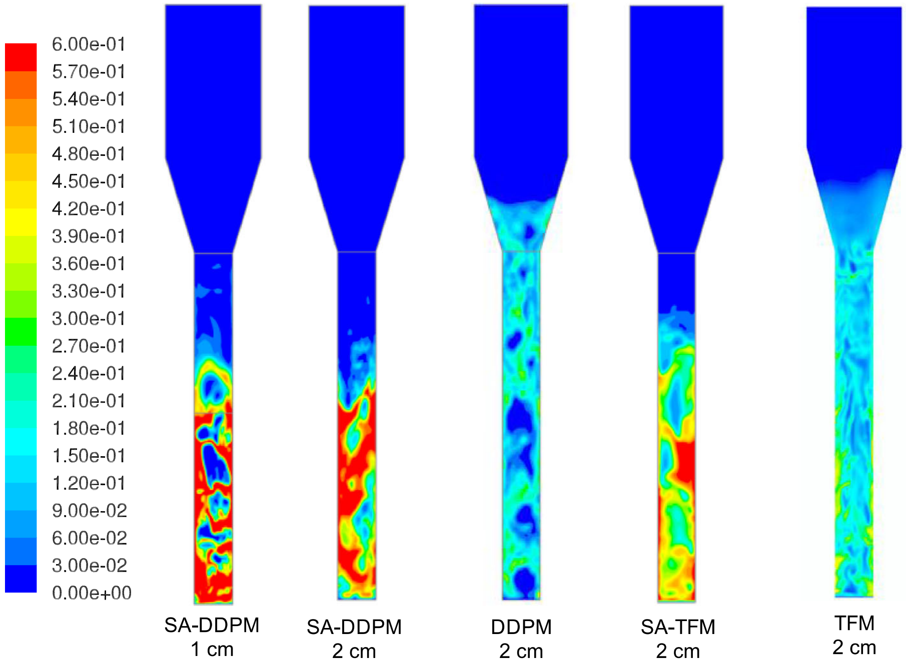

Figure 4. Snapshots of the solids volume fraction at $t = 20$ s for pilot-scale bubbling fluidized bed ($W_g^{\mathrm{in}} = 0.4\,\mathrm{m\,s^{-1}}$). The SA-TFM results are taken from Schneiderbauer[53,55] and the standard TFM results are deduced from Cloete et al.[70]

In **Figure 5**a, the time-averaged axial pressure gradient for a superficial gas velocity $W_g^{\text{in}} = 0.4\,\text{m}\,\text{s}^{-1}$ is shown. Here, the time averaging was used over 20 s of simulation time. This time averaging interval window was large enough to obtain time-independent mean values.[53,55] The figure clearly shows that using standard DDPM considerably underestimates the axial pressure gradient as the gas–solid drag force does not account for the unresolved heterogeneous structures.[55,70] In contrast, the SA-DDPM model appropriately predicts the pressure gradient even though the grid spacing is nearly two orders of magnitude larger than the grid resolution required for a TFM approach.[55]

Figure 5b shows the time-averaged radial solids volume fraction at $z = 0.6$ m. The figure reveals that the SA-DDPM correctly predicts the radial profile of the solids volume fraction. Furthermore, the degree of the segregation of the solid phase in the vessel is in fairly good agreement with the experimental data. As already observed from Figure 5a, using standard DDPM without considering the effect of subgrid structures yields to a considerable underestimation of the solids holdup.

In addition, in Figure 4 and 5 numerical predictions obtained from the SA-DDPM approach using different grid resolutions are shown. The results clearly unveil that the present numerical method is rather insensitive to the grid resolution. However, it has to be emphasized that decreasing the grid spacing by a factor 2 requires an increase in the number of parcels approximately by a factor 8. Finally, in Figure 4 and 5 results obtained from kinetic theory-based TFM and SA-TFM simulations are presented. These results are taken from refs. [53,55,70]. Comparing DDPM and TFM simulations as well as SA-DDPM and SA-TFM simulations yields nearly equivalent predictions. Thus, it can be concluded that for coarse grid simulations subgrid model is required and furthermore, subgrid models developed for TFM can be used for Euler–Lagrangian approaches as well.[40]

4.2. Iron Ore Reduction in Lab-Scale Fluidized Bed

The reduction model presented in Section 2.3 has already applied successfully to the direct reduction of iron ore in the context of CFD-DEM[16] in our previous study.[12] To verify its implementation in the SA-DDPM approach, we investigate the direct reduction of hematite ore within a lab-scale fluidized bed with 68 mm diameter.[69] **Figure 6** shows snapshots of the solid volume fraction, the mass fraction of H_2, the mass fraction of H_2O, and the fractional reduction of individual parcels during the conversion of wustite to iron (R1, Table 1). On the one hand, Figure 6a shows that the bed is operated in the bubbling regime closely to the minimum fluidization velocity. Fluidization considerably increases mixing, the gas-solid contact, and the reaction heat removal. On the other hand, Figure 6b,c clearly shows the consumption of H_2 and the production of H_2O due to the conversion of wustite to iron. Furthermore, Figure 6d shows that the heavier ore particles tend to segregate from the lighter sand particles to the bottom of the fluidized bed. Comparing Figure 6a,d suggests that regions with a higher fraction of ore particles defluidize due to the low superficial gas velocity.

In **Figure 7**, the fractional reduction as a function of time for the different reduction steps and different particle diameters is plotted. Both experiment and simulation unveil that the conversion of hematite to magnetite (R3) is the fastest reduction step.[71] After approximately 1 min the fractional reduction of the smallest particle fraction approaches a plateau, where the fractional reduction is about 11.1%. Here, the total amount of hematite was already converted to magnetite. In contrast, for the largest particle fraction ($d_4 = 0.75$ mm), the full conversion to magnetite takes about 5 min. The subsequent conversion from magnetite to wustite is known to be the second fastest reduction step, which is also correctly predicted by the presented conversion model. Again, the fractional reduction approaches a plateau region after 6–7 min, where the fraction reduction is about 33.3%, which is in fairly good agreement with the experiment. Similar to R3, the smallest particle fraction is converted considerably faster than larger particles. Thus, appropriate modeling of the particle size distribution is necessary to correctly predict the reduction speed. The final reduction step, where wustite is converted to metallic iron, unveils the slowest conversion rate. Similar to the previous reduction steps, the present model is able to correctly predict the conversion of wustite to iron.

Figure 8 shows snapshots of the parcel positions at the beginning of R1, where the parcels are colored by the particle diameter and the actual fractional reduction. The figure shows that larger particles segregate to the bottom of the bed, whereas the smaller

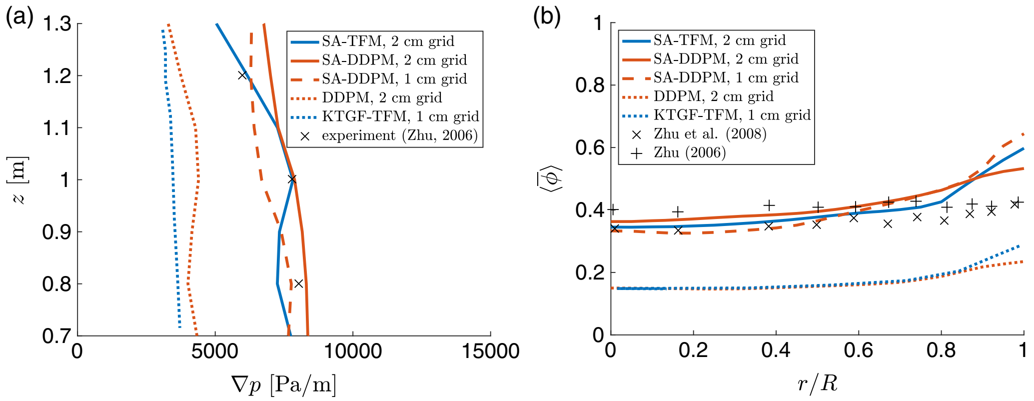

Figure 5. a) Time-averaged pressure gradient as a function of the vertical coordinate, z, for pilot-scale bubbling fluidized bed ($W_g^{\text{in}} = 0.4\,\text{m}\,\text{s}^{-1}$); b) time-averaged solids volume fraction as a function of the radial coordinate, r/R, at $z = 0.6$ m. The SA-TFM results are taken from Schneiderbauer [55] and the standard TFM results are deduced from Cloete et al.[70]

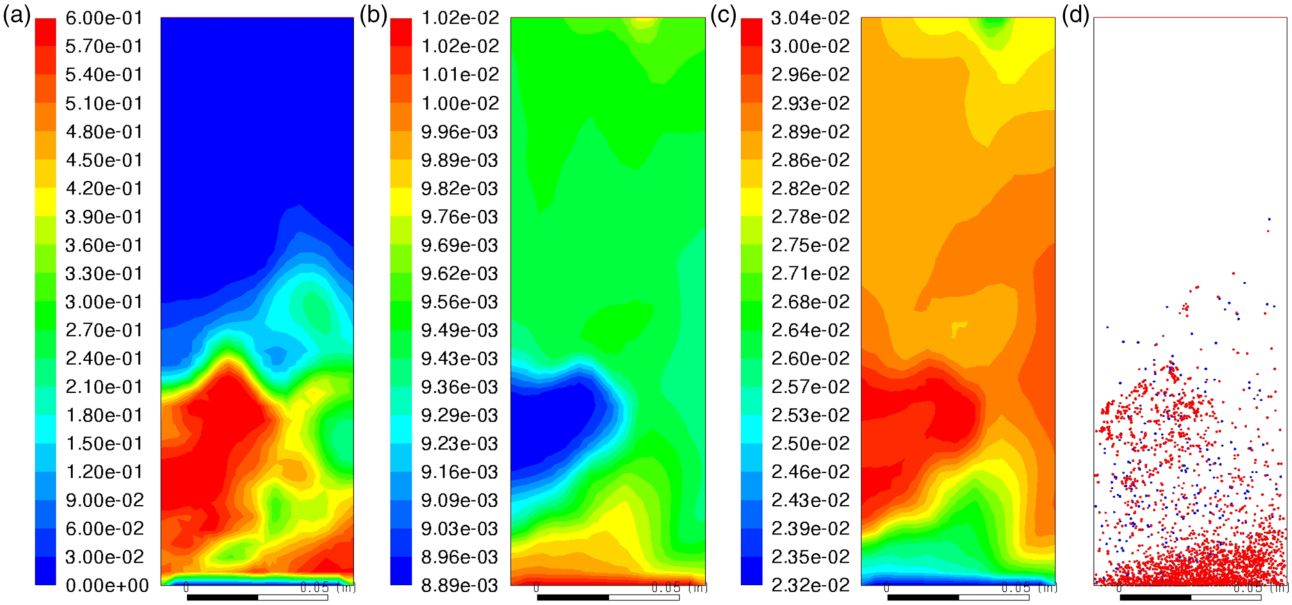

Figure 6. Snapshots at the beginning of R1 of a) the solid volume fraction, b) the mole fraction of H_2, c) the mole fraction of H_2O, and d) the particle type (blue: sand, red: ore).

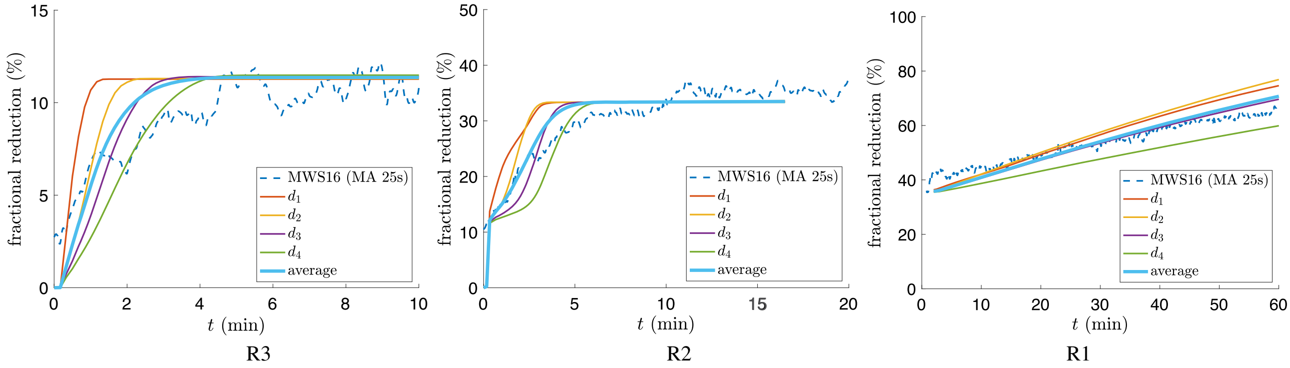

Figure 7. Fractional reduction as a function of time for different particle sizes ($d_1 = 0.094$ mm, $d_2 = 0.1875$ mm, $d_3 = 0.375$ mm, $d_4 = 0.75$ mm).

particles remain fluidized. Furthermore, these smaller particles show a higher reduction degree and appear to consume more reducing agents (compare with Figure 6b).

Finally, **Figure 9** shows the total time series of the fractional reduction. Here, the fractional reduction is computed for all particle size fractions. Here, it has to be emphasized that the simulations were stopped after reaching the plateaus during R3 and R2 to reduce the computational demands. Afterward, the simulations were restarted at the beginning of R2 and R1. Furthermore, the figure clearly demonstrates that the current SA-DDPM approach together with a particle (parcel)-based reduction model reveals fairly good agreement with experimental data.

4.3. Iron Ore Reduction in Industrial-Scale Fluidized Bed

In this section, the hydrodynamics and the reduction characteristics of an industrial-scale fluidized bed are discussed. **Figure 10**a and **11**a show a snapshot of the particle volume fraction during R3 (Table 1). The figure reveals that the bed is well fluidized using a grid of spouts (Figure 2b). Furthermore, the cyclone diplec appears to prevent the flow to enter the cyclone from the bottom. Furthermore, Figure 11b shows the parcel positions near the symmetry plane corresponding to the particle volume fraction, as shown in Figure 11a. The parcels are colored by their corresponding particle diameter. The figure shows that inside the fluidized bed no distinct segregation occurs. Thus, the different particle size fractions are well mixed inside the bed. However, smaller particles whose terminal settling velocity is smaller than the superficial gas flow are entrained to the freeboard. These particles are mostly separated by the cyclone and fed back to the fluidized bed. Figure 3a shows that solely the smallest size fractions ($d_p < 2\,\mu$m) are found in the offgas of the cyclone, whereas in the freeboard particles up to a diameter of 100 μm are found. Figure 3a clearly shows further that the numerical predictions of the particle size distributions in the freeboard and the offgas are in fairly good agreement with plant data.

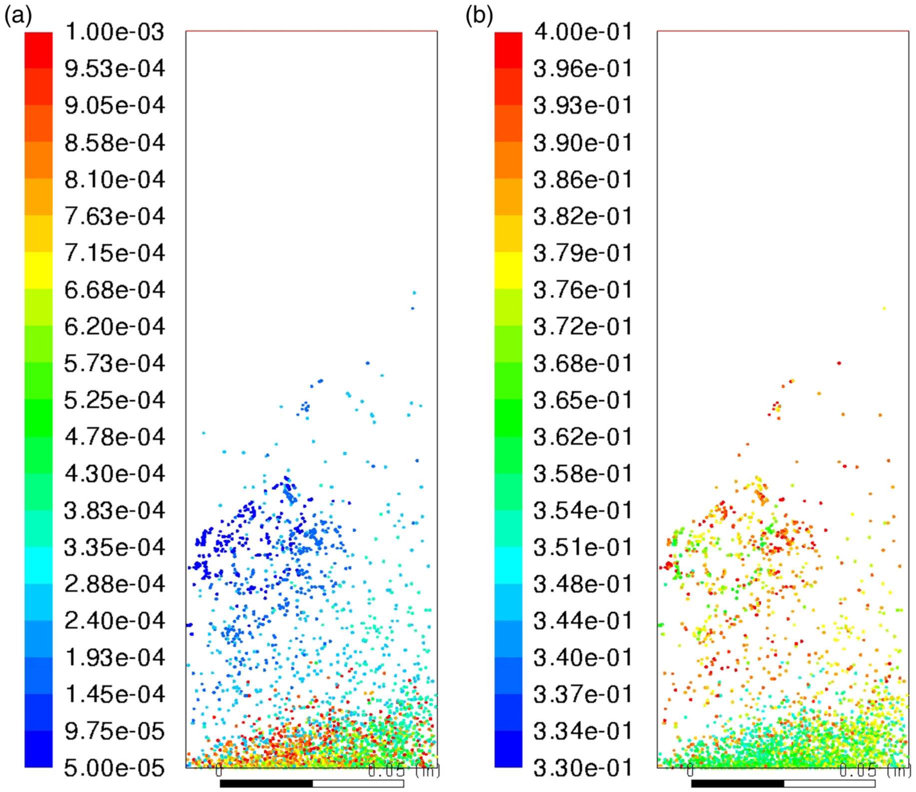

Figure 8. Snapshots at the beginning of R1 of a) the particle diameter and b) the fractional reduction. Note that only the ore parcels are shown here.

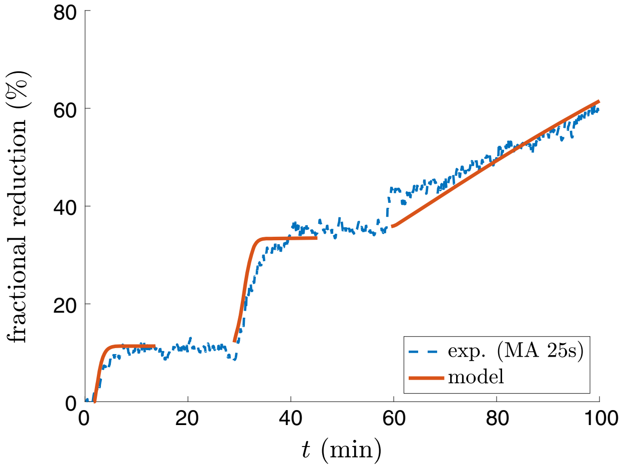

Figure 9. Average fractional reduction as a function of time for the different reduction steps.

Figure 12 shows the average voidage inside the bed region and the average mass-loading near the cyclone inlet as a function of time. While the average voidage is correctly predicted during the steady-state operation of the fluidized bed, the average mass-loading of the freeboard is overpredicted. This can be explained by the uncertainties in the determination of the initial particle size distribution. The smallest size fraction experimentally available for the initial size distribution was 63 μm. Thus, the initial fraction of smaller particles, which are present in the freeboard and offgas measurements, had to be extrapolated. Minor errors introduced during this extrapolation considerably affect the mass-loading in the freeboard.

In **Figure 13** snapshots of the particle parcel positions are presented, where the parcels are colored by their primary diameter and by their actual fractional reduction. As already discussed thoroughly smaller particles are converted much faster from hematite to magnetite. Thus, in the freeboard nearly all particles are already fully converted, while in the bed the larger particles show much lower conversion. Comparing Figure 10 and 13 shows that in dense areas of the fluidized bed the complete amount of reducing agents is consumed, whereas within the bubbles no considerable reduction of the reactants can be observed. Thus, there are two limiting effects for the reaction rates. On the one hand, the chemical reaction path is outlined in Section 2.3 and on the other hand, the local availability of reducing agents. The latter is mostly determined by the gas supply from the bottom as well as the reactant diffusion between voids and dense areas.

Finally, in Figure 3b the fractional reduction for the different particle diameters is plotted. The figure shows the particles smaller than 100 μm are nearly immediately converted (in less than 1 min). In contrast, for the largest particles (larger than 1 mm) the full conversion takes between 5 and 20 min. Comparing Figure 3b, 7, and 9 shows that although the gas compositions for the lab-scale and industrial-scale fluidized beds are different, on average particles of the same size are converted at nearly the same rate in both cases. To conclude, the current

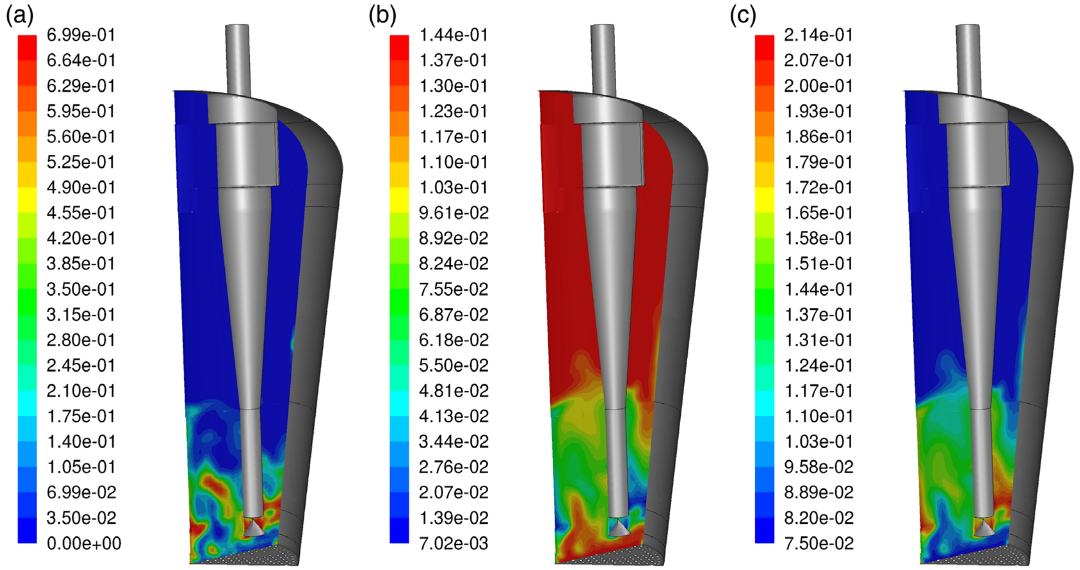

Figure 10. Snapshots during R3 of a) the solid volume fraction, b) the mole fraction of H_2, and c) the mole fraction of H_2O and the fractional reduction for the industrial-scale fluidized bed.

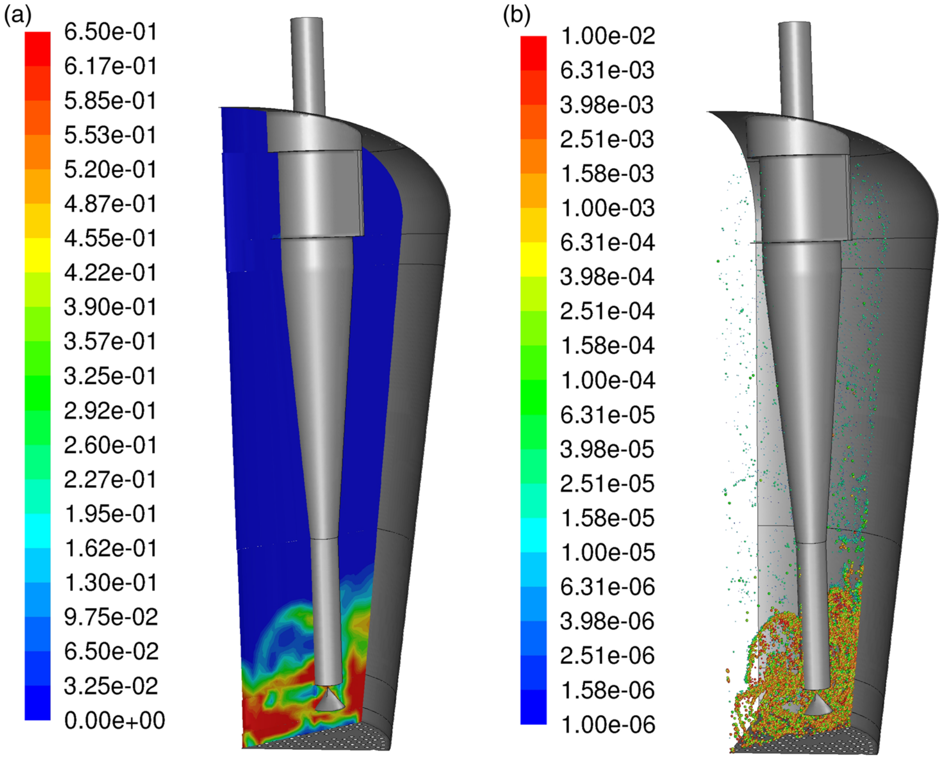

Figure 11. Snapshots at the end of R3 of a) the solid volume fraction and b) particle diameter for the industrial-scale fluidized bed.

approach appears to be an appropriate tool for the numerical assessment of the reduction of iron ores in fluidized beds, although the impact of subgrid heterogeneities on the heat and mass transfer has been neglected in this study. However, future work will concentrate on evaluating their contribution thoroughly.[56,72,73]

5. Conclusion

In this article, we presented a generalized Euler–Lagrange approach for the assessment of the direct reduction of iron ore in large-scale fluidized beds. This method includes 1) subgrid models accounting for unresolved structures in the case of coarse

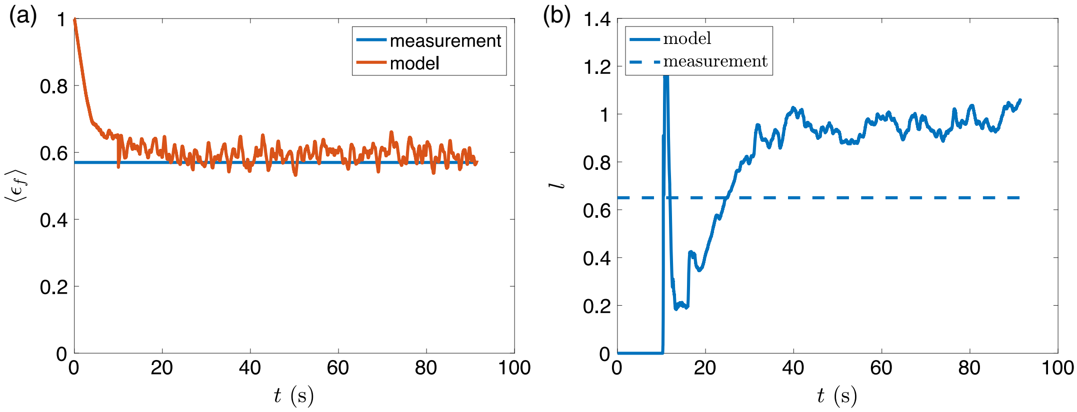

Figure 12. a) Average voidage inside the bed region as a function of time for the industrial-scale fluidized bed; b) average particle mass loading near the cyclone inlet.

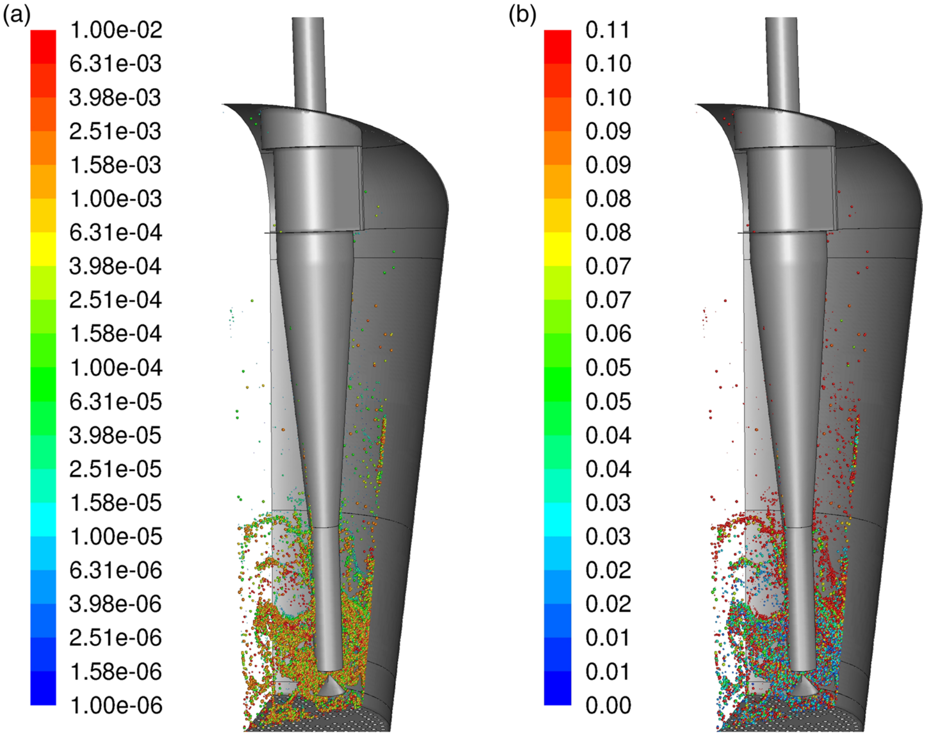

Figure 13. Snapshots during R3 of a) particle diameter and b) the fractional reduction for the industrial-scale fluidized bed (the snapshots are taken at the same time as Figure 11).

grid resolutions[51,52] and 2) a particle-based unreacted shrinking core reduction model picturing the conversion of iron ores to iron.[1,12] Such a modeling strategy enables the efficient numerical analysis of reactive polydisperse gas-phase reactors without requiring computationally demanding multifluid models, which are coupled to population balance approaches.

To conclude, the results clearly show that the reactive SA-DDPM is able to picture the correct conversion rates within the fluidized bed. Furthermore, it is once again shown that the rate determining step is the wustite to iron reduction, which is underlined by the polydisperse lab-scale fluidized bed simulations being in good agreement with experiments.

Nevertheless, the conversion model has to be verified further against more different gas compositions. Thus, future efforts will concentrate on the numerical analysis of different process conditions and their detailed evaluation against experimental data. Finally, subgrid corrections for heat and mass transfer[56] may be required to account for the unresolved small scales on the conversion rates.

Acknowledgements

The financial support by the Austrian Federal Ministry for Digital and Economic Affairs and the National Foundation for Research, Technology and Development is gratefully acknowledged. The authors further want to acknowledge the funding support of K1-MET GmbH, metallurgical competence center. The research program of the K1-MET competence center is supported by COMET (Competence Center for Excellent Technologies), the Austrian program for competence centers. COMET is funded by the Federal Ministry for Transport, Innovation and Technology, the Federal Ministry for Digital and Economic Affairs and the provinces of Upper Austria, Tyrol and Styria. Apart from the public funding from COMET, this research project is partially financed by the industrial partners Primetals Technologies Austria GmbH, voestalpine Stahl Donawitz GmbH, RHI Magnesita GmbH and voestalpine Stahl GmbH.

Conflict of Interest

The authors declare no conflict of interest.

Keywords

dense discrete phase model, FINEX, fluidized bed, iron ore reduction, subgrid models

Received: April 29, 2020
Revised: June 2, 2020

[1] M. S. Valipour, *Trans. C Chem. Chem. Eng.* **2009**, *16*, 108.
[2] J. Schenk, *Particuology* **2011**, *9*, 14.
[3] A. Habermann, F. Winter, H. Hofbauer, J. Zirngast, J. L. Schenk, *ISIJ Int.* **2000**, *40*, 935.
[4] Primetals Technologies Austria GmbH, POSCO E&C. The Finex Process. https://www.primetals.com/fileadmin/user_upload/content/01_portfolio/1_ironmaking/finex/The_Finex_process.pdf, p. 15 (accessed: April 2020).
[5] F. J. Plaul, C. Böhm, J. L. Schenk, *J. South. African Inst. Min. Metall.* **2009**, *109*, 121.
[6] S. Natsui, T. Kikuchi, R. O. Suzuki, *Metall. Mater. Trans. B* **2014**, *45*, 2395.
[7] S. Natsui, S. Ueda, H. Nogami, J. Kano, R. Inoue, T. Ariyama, *Chem. Eng. Sci.* **2012**, *71*, 274.
[8] M. S. Valipour, M. Y. Motamed Hashemi, Y. Saboohi, *Adv. Powder Technol.* **2006**, *17*, 277.
[9] D. Fu, C. Q. Zhou, Y. Chen, *J. Therm. Sci. Eng. Appl.* **2014**, *6*, 021014.
[10] E. Dianyu, *Particuology*, **2020**, *51*, 163.
[11] S. Schneiderbauer, M. E. Kinaci, F. Hauzenberger, S. Pirker, in *Prog. Appl. CFD – CFD2017 Proc. 12th Int. Conf. Comput. Fluid Dyn. Oil Gas, Metall. Process Ind.*, SINTEF, Trondheim, Norway **2017**, pp. 97–105.
[12] M. E. Kinaci, T. Lichtenegger, S. Schneiderbauer. *Chem. Eng. Sci.*, **2020**, *227*, 115858.
[13] B. Peters, F. Hoffmann, *Chem. Eng. J.* **2016**, *304*, 692.
[14] B. Peters, F. Hoffmann, D. Senk, A. Babich, *Chem. Eng. Sci.* **2016**, *140*, 189.
[15] M. Baniasadi, B. Peters, J. C. Pierret, B. Vanderheyden, O. Ansseau, *Powder Technol.* **2018**, *339*, 863.
[16] C. Goniva, C. Kloß, A. Hager, G. Wierink, S. Pirker, in *Proc. 8th Int. Conf. CFD Oil Gas, Metallurgical Process Industries*, SINTEF, Trondheim, Norway **2011**, p. 9.
[17] S. Pirker, C. Goniva, C. Kloss, S. Puttinger, J. Houben, S. Schneiderbauer, *Powder Technol.* **2012**, *235*, 572.
[18] C. K. K. Lun, S. B. Savage, D. J. Jeffrey, N. Chepurniy, *J. Fluid Mech.* **1984**, *140*, 223.
[19] S. Schneiderbauer, A. Aigner, S. Pirker, *Chem. Eng. Sci.* **2012**, *80*, 279.
[20] K. Agrawal, P. N. Loezos, M. Syamlal, S. Sundaresan, *J. Fluid Mech.* **2001**, *445*, 151.
[21] H. Iddir, H. Arastoopour, *AIChE J.* **2005**, *51*, 1620.
[22] D. Schellander, S. Schneiderbauer, S. Pirker, *Chem. Eng. Sci.* **2013**, *95*, 107.
[23] S. Schneiderbauer, S. Puttinger, S. Pirker, P. Aguayo, V. Kanellopoulos, *Chem. Eng. J.* **2015**, *264*, 99.
[24] ANSYS. *ANSYS Fluent Theory Guide (v19.2)*, ANSYS, Inc., Canonsburg, PA **2018**, pp. 1–860.
[25] S. Cloete, S. Amini, in *Proc. 9th Int. Conf. on Multiphase Flow*, **2016**, pp. 1–7.
[26] J. Chen X., *Powder Technol.* **2014**, *254*, 94.
[27] E. M. Ryan, D. DeCroix, R. Breault, W. Xu, E. D. Huckaby, K. Saha, S. Dartevelle, X. Sun, *Powder Technol.* **2013**, *242*, 117.
[28] W. P. Adamczyk, A. Klimanek, R. A. Bialecki, G. Wecel, P. Kozolub, T. Czakiert, *Particuology* **2014**, *15*, 129.
[29] W. P. Adamczyk, P. Kozołub, A. Klimanek, R. A. Białecki, M. Andrzejczyk, M. Klajny, *Appl. Therm. Eng.* **2015**, *87*, 127.
[30] A. Klimanek, W. P. Adamczyk, A. Katelbach-Wozniak, G. Wecel, A. Szlek, *Fuel* **2015**, *152*, 131.
[31] S. Pirker, D. Kahrimanovic, C. Kloss, B. Popoff, M. Braun, *Powder Technol.* **2010**, *204*, 203.
[32] M. Massoudi Farid, H. J. Jeong, K. H. Kim, J. Lee, D. Kim, *Fuel* **2017**, *192*, 187.
[33] S. Kraft, F. Kirnbauer, H. Hofbauer, *Appl. Energy* **2017**, *190*, 408.
[34] D. M. Snider, *J. Comput. Phys.* **2001**, *170*, 523.
[35] P. J. O'Rourke, D. M. Snider, *Chem. Eng. Sci.* **2010**, *65*, 6014.
[36] P. J. O'Rourke, D. M. Snider, *Chem. Eng. Sci.* **2012**, *80*, 39.
[37] S. Radl, C. Radeke, J. G. Khinast, S. Sundaresan, in *Proc. 8th Int. Conf. on CFD Oil Gas, Metallurgical and Process Industries*, SINTEF, Trondheim, Norway **2011**, pp. 1–10.
[38] S. Radl, S. Sundaresan, *Chem. Eng. Sci.* **2014**, *117*, 416.
[39] F. Li, F. Song, S. Benyahia, W. Wang, J. Li, *Chem. Eng. Sci.* **2012**, *82*, 104.
[40] S. Benyahia, S. Sundaresan, *Powder Technol.* **2012**, *220*, 2.
[41] S. Schneiderbauer, S. Puttinger, S. Pirker, *AIChE J.* **2013**, *59*, 4077.
[42] S. Schneiderbauer, S. Pirker, *AIChE J.* **2014**, *60*, 839.
[43] Y. Igci, A. T. Andrews, S. Sundaresan, S. Pannala, T. J. O'Brien, *AIChE J.* **2008**, *54*, 1431.
[44] C. C. Milioli, F. E. Milioli, W. Holloway, K. Agrawal, S. Sundaresan, *AIChE J.* **2013**, *59*, 3265.
[45] A. Sarkar, F. E. Milioli, S. S. Ozarkar, T. Li, X. Sun, S. Sundaresan, *Chem. Eng. Sci.* **2016**, *152*, 443.
[46] J.-F. Parmentier, O. Simonin, O. Delsart, *AIChE J.* **2012**, *58*, 1084.
[47] A. Ozel, P. Fede, O. Simonin, *Int. J. Multiph. Flow* **2013**, *55*, 43.
[48] B. Lu, W. Wang, *Chem. Eng. Sci.* **2009**, *64*, 3437.
[49] J. Wang, M. A. van der Hoef, J. A. M. Kuipers, *Chem. Eng. Sci.* **2010**, *65*, 2125.
[50] A. Ozel, J. Kolehmainen, S. Radl, S. Sundaresan, *Chem. Eng. Sci.* **2016**, *155*, 258.
[51] S. Schneiderbauer, *AIChE J.* **2017**, *63*, 3544.
[52] S. Rauchenzauner, S. Schneiderbauer, *Int. J. Multiph. Flow* **2020**, *126*, 103237.
[53] S. Schneiderbauer, *Chem. Eng. Technol.* **2020**, *43*, 848.
[54] S. Schneiderbauer, *AIChE J.* **2018**, *64*, 1591.
[55] S. Schneiderbauer, *AIChE J.* **2018**, *64*, 1606.
[56] S. Rauchenzauner, S. Schneiderbauer. *Phys. Fluids* **2020**, *32*, 063307.
[57] S. Schneiderbauer, M. Saeedipour, *Phys. Fluids* **2018**, *30*, 023301.
[58] S. Schneiderbauer, M. Saeedipour, *Int. J. Multiph. Flow* **2019**, *114*, 287.
[59] D. J. Gunn, *Int. J. Heat Mass Transf.* **1978**, *21*, 467.
[60] R. Beetstra, M. A. Van der Hoef, J. A. M. Kuipers, *AIChE J.* **2007**, *53*, 489.

[61] M. A. van der Hoef, M. van Sint Annaland, N. G. Deen, J. A. M. Kuipers, *Annu. Rev. Fluid Mech.* **2008**, *40*, 47.

[62] C. Goniva, C. Kloss, N. G. Deen, J. A. M. Kuipers, S. Pirker, *Particuology* **2012**, *10*, 582.

[63] C. Kloss, C. Goniva, A. Hager, S. Amberger, S. Pirker, *Fluid Dyn.* **2012**, *12*, 140.

[64] A. Stroh, F. Alobaid, M. T. Hasenzahl, J. Hilz, J. Ströhle, B. Epple, *Particuology* **2016**, *29*, 34.

[65] W. D. Fullmer, C. M. Hrenya, *AIChE J.* **2016**, *61*, 11.

[66] J. H. Cloete, S. Cloete, F. Municchi, S. Radl, S. Amini, *Chem. Eng. Sci.* **2018**, *192*, 930.

[67] Q. T. Tsay, W. H. Ray, *AIChE J.* **1976**, *22*, 1064.

[68] H. Zhu, J. Zhu, G. Li, F. Li, *Powder Technol.* **2008**, *180*, 339.

[69] D. Spreitzer, *Optimierung der Prozessparameter für die Reduktion von Feineisenerzen mittels Wirbelschichtverfahren.* **2016**.

[70] S. Cloete, S. T. Johansen, S. Amini, *Powder Technol.* **2013**, *235*, 91.

[71] M. B. Hanel, J. F. Schenk, H. Mali, F. Hauzenberger, C. Thaler, H. Stocker, *BHM Berg- und Hüttenmännische Monatshefte* **2015**, *160*, 316.

[72] K. Agrawal, W. Holloway, C. C. Milioli, F. E. Milioli, S. Sundaresan, *Chem. Eng. Sci.* **2013**, *95*, 291.

[73] W. Holloway, S. Sundaresan, *Chem. Eng. Sci.* **2012**, *82*, 132.